Site-Specific Sodiation Mechanisms of Selenium in Microporous Carbon Host

Frédéric A. Perras,[*1] Sooyeon Hwang,[2] Yixian Wang,[3] Ethan C. Self,[4] Pengcheng Liu,[3] Rana Biswas,[1,5,6] Sudhan Nagarajan,[3] Viet Hung Pham,[3] Yixin Xu,[2,7] J. Anibal Boscoboinik,[2] Dong Su,[2] Jagjit Nanda,[4] Marek Pruski,[1,8] and David Mitlin[*3]

[1] US DOE, Ames Laboratory, Ames, IA, 50011

[2] Center for Functional Nanomaterials, Brookhaven National Laboratory, Upton, NY, 11973, USA

[3] Materials Science and Engineering Program & Texas Materials Institute, The University of Texas at Austin, Austin, TX, 78712

[4] Chemical Sciences Division, Oak Ridge National Laboratory, Oak Ridge, TN, 37831, USA

[5] Microelectronics Research Center, Department of Electrical and Computer Engineering, Iowa State University, Ames, IA, 50011

[6] Department of Physics and Astronomy, Iowa State University, Ames, IA, 50011

[7] Materials Science and Chemical Engineering Department, Stony Brook University, Stony Brook, NY, 11790, United States

[8] Department of Chemistry, Iowa State University, Ames, IA, 50011

KEYWORDS: sodium-sulfur batteries, lithium-sulfur batteries, selenides, sodium metal batteries (SMBs), lithium metal batteries (LMBs), solid-state NMR

Abstract

We combined advanced TEM (HRTEM, HAADF, EELS) with solid-state (SS)MAS NMR and electroanalytical techniques (GITT, *etc.*) to understand the site-specific sodiation of selenium (Se) encapsulated in a nanoporous carbon host. The architecture employed is representative of a wide number of electrochemically stable and rate-capable Se-based sodium metal battery (SMB) cathodes. SSNMR demonstrates that during first sodiation, the Se chains are progressively cut to form an amorphous mixture of polyselenides of varying lengths, with no evidence for discrete phase transitions during sodiation. It also shows that Se nearest the carbon pore surface is sodiated first, leading to the formation of a core-shell compositional profile. HRTEM indicates that the vast majority of the pore confined Se is amorphous, with only localized presence of nanocrystalline equilibrium Na_2Se_2 (hcp) and Na_2Se (fcc). Nanoscale fracture of terminally sodiated Na-Se is observed by HAADF, with SSNMR indicating a physical separation of some Se from the carbon host after the first cycle. GITT reveals a threefold increase in Na^+ diffusivity at cycle two, which may be explained by the creation of extra interfaces. These combined findings highlight the complex phenomenology of electrochemical phase transformations in nanoconfined materials, which may profoundly differ from their "free" counterparts.

Text

Researchers are actively pursuing metal batteries (MBs), which have the potential to provide more than twice the energy of conventional lithium/sodium ion battery (LIB/SIB) architectures. The principle behind MBs is to employ a high-capacity cathode (*e.g.* Se, S, S-Se, LiNiMnCo (NMC), *etc.*) opposite a metal Li/Na anode.[1-4] The key argument for Na versus Li is a geo-economic one, as the precursors for Na-based batteries are universally abundant, including from land-based sources (NaCl salt, sodium carbonate, sodium hydroxide) and from sea water. Both sodium ion batteries (SIBs) and sodium metal batteries (SMBs) can employ an inexpensive aluminum current collector for either electrode, since it is Na-inert. SMBs are quite new and pose significant challenges due to the reactive nature of the Na metal. However, recent work has demonstrated the stability of Na metal anodes in “classic” carbonate-based

electrolytes.[5, 6] This opens the possibility of safe and cyclically-stable SMBs. Advances in sodium-sulfur SMB systems have been made,[7-10] although in this case there is the ongoing issue of low reactivity between solid S and Na at room temperature.

Selenium (Se) possesses electrochemical properties that are superior to those of sulfur, including orders of magnitude higher electrical conductivity and more facile sodiation/lithiation kinetics. It may exist in at least four allotropes: trigonal, amorphous, monoclinic, and hexagonal, which vary in electrical conductivity. Selenium with an equilibrium trigonal structure has an electrical conductivity on the order of 10^{-3} S m^{-1}, while amorphous Se has conductivity on the order of 10^{-11} S m^{-1}.[11, 12] For comparison, the conductivity of crystalline sulfur is on the order of 10^{-27} S m^{-1}. Although Se has a lower gravimetric capacity with Li/Na than S (Li_2Se = Na_2Se = 675 mAh g^{-1}, Li_2S = 1675 mAh g^{-1}), it has comparable volumetric capacity (Li_2Se = Na_2Se = 3250 mAh cm^{-3}, Li_2S = 3470 mAh cm^{-3}). While Na-Se SMBs operate at lower voltage than conventional NIBs (*e.g.* ~ 1.6 V vs. 3.5 V), they remain quite promising due to the very high capacity of both the cathode and the metal anode (1166 mAh g^{-1}), as well as their superior kinetics and capacity utilization versus sodium-sulfur systems.

Overall, it is unlikely that a pure-Se based batteries will ultimately see commercialization. Pure selenium is not an element found naturally in nature, rather being obtained by purifying byproducts of various mining operations or being separated from sulfur deposits. Despite its relatively low cost (~ $ 20 per kg), pure Se is not widely available. Where Se is likely to have a foothold, however, is as an additive to S-based cathodes. For example, selenium sulfide (SeS_2) is an anti-fungal agent that is widely commercially available at $ 15 - 20 per kilogram. The compound SeS_2 is a byproduct of sulfur mining, being naturally present in sulfur ore. It also occurs when sulfur is removed from mining water or from petroleum processing, *e.g.* Canadian Tar Sands Tailings. Selenium sulfide may be added to a S-based cell to boost its electrical conductivity and reaction kinetics.[13-16] Similar to the evolution of toxic H_2S from a rapidly and uncontrollably heated Li-S cell, the evolution of H_2Se can create safety concerns.

Scientifically, Se-based SMBs are interesting due to their novelty and the wide array of as-yet unexplored electrochemical sodiation reactions. In particular, the

understanding of the Na-Se electrochemical reactions is in its infancy. Recent *in-situ* TEM analysis performed on unsupported crystalline (equilibrium trigonal) Se nanowires suggested the presence of Na_2Se_2 (hexagonal, $P6_3/mmc$) during the slow *in-situ* sodiation sequence, and an amorphous Na_xSe at lower Na content.[17] However, this was a "dry" (no electrolyte) *in-situ* configuration with free standing, rather than carbon-supported wires desodiated at an unspecified current density and voltage. There has also been work on isolated Se molecules filling the insides of nanotubes.[18] While this is a highly interesting low-mass loading architecture, it is far from a realistic application for battery electrodes with much higher Se mass loadings and larger pore sizes. High-performance Na-Se cathodes are based on high-mass loading (40 wt.% or more) of amorphous Se phase, which forms at intermediate solidification rates or when impregnated into nanopores.[18-21] Some trigonal-based Se-Na electrodes have also been reported.[17]

A key problem in understanding the relevant sodiation reactions is that technologically promising Se-, S- and SeS-based cathodes consist of high-mass-loading active phases impregnated into three-dimensional microporous carbon hosts. Coarse-grained techniques such as electroanalytical methods or X-ray diffraction techniques are unable to capture the site-specific details of the phase transformations within the carbon's micropores. Advanced transmission electron microscopy (TEM), on the other hand, is suited for probing sodiation phase transformations locally, given its ability to simultaneously obtain structure and bonding information with near-atomic-scale site-specificity.[22-25] In parallel, ^{77}Se solid-state nuclear magnetic resonance spectroscopy (SSNMR) is sensitive to the level of reduction and the composition of polyselenides in materials, and providing an atomistic probe for the state of charge.[26-35] The formation of nanoscale crystalline domains within the micropores of the carbon material could be assessed using ^{23}Na SSNMR spectroscopy, as it is sensitive to crystal packing.[36-38] The objective of the current work is to understand the Se sodiation reactions inside the micropores of a model carbon host, employing TEM and SSNMR combined with a suite of complementary electroanalytical and analytical methods. The fundamental findings from this work should be applicable to a wide-range of Se in nanoporous carbon host architectures found in battery materials literature.[39-41]

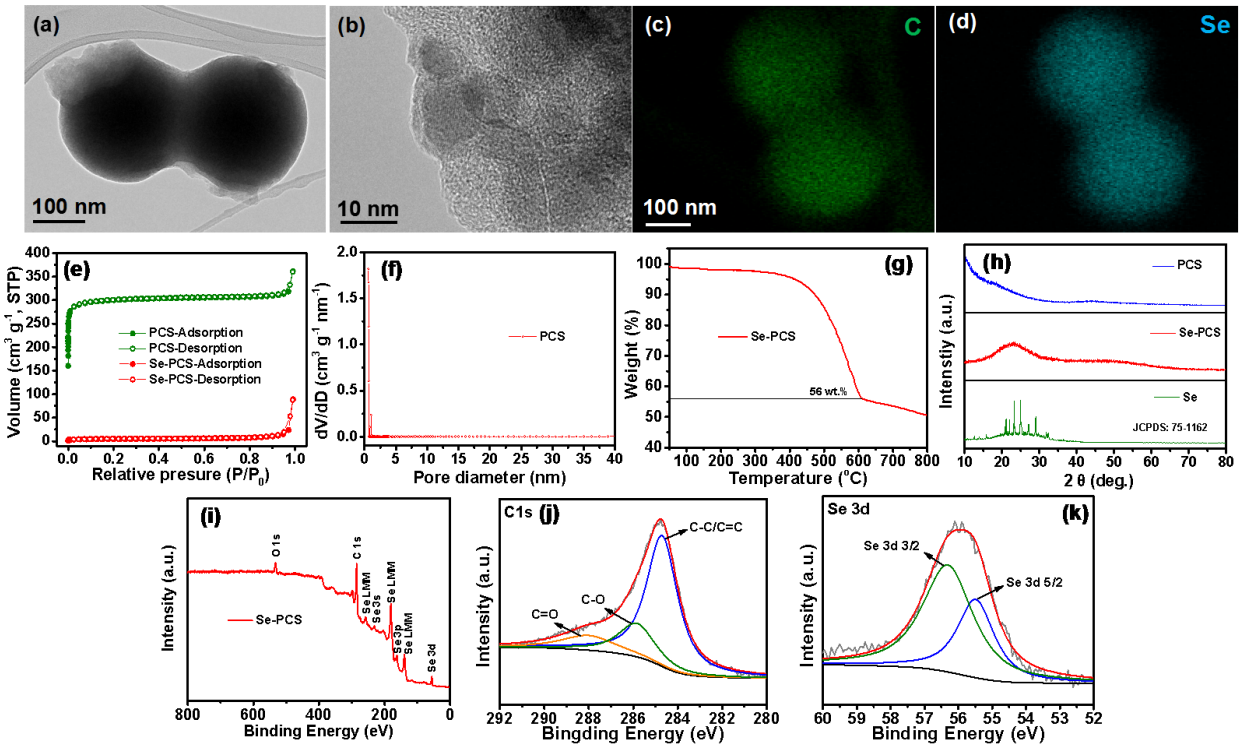

Figure 1. (a, b) TEM and HRTEM images of Se-PCS. (c, d) EDXS elemental maps of C and Se. (e) Nitrogen adsorption-desorption isotherms of PCS host and Se-PCS. (f) Pore size distribution of the PCS host. (g) Thermogravimetric curve of Se-PCS. (h) XRD patterns of as-received PCS, Se-PCS and Se. (i) XPS survey spectrum of Se-PCS. (j, k) High resolution XPS spectra of C 1s and Se 3d.

Model porous carbon spheres (PCS) were synthesized from D-glucose by hydrothermal synthesis followed by simultaneous carbonization-KOH activation. Selenium was then loaded into the pores of the PCS though a single-step impregnation-anneal at 260 °C, yielding Se-PCS. **Figures S1(a) and (b)** show SEM images of PCS and Se-PCS, respectively. The materials are morphologically analogous, being agglomerated arrays of spheres with an average size of 200 nm. This is indicated by the particle size distribution provided as an inset in **Fig. S1(a)**. **Figure 1(a)** shows a bright-field TEM image further highlighting the morphology of Se-PCS. The surface of the spheres is relatively smooth, without obvious crystalline features. As will be demonstrated, the Se is primarily embedded inside the carbon, rather than "spilling out" onto the surface. **Figure 1(b)** shows a higher magnification image of several Se-PCS particles, with the Se-rich regions being darker due to a combination of diffraction and mass-thickness contrast. **Figures 1(c)** and **(d)** show energy-dispersive X-ray (EDX) C and Se maps for another set of particles. It may be observed that the Se is uniformly dispersed within its carbon host, indicating uniform loading throughout the carbon matrix. Generally, through the comparison between the TEM images and EDX maps,

it can be concluded that the Se distribution is quite uniform. There is no detectable evidence of stray Se particles/islands/crystallites attached on or near the PCS surfaces.

Figure 1(e) shows the Brunauer-Emmett-Teller (BET) data for the as-synthesized PCS and for Se-PCS. The adsorption curve of PCS displays a type I isotherm, associated with microporous materials. The calculated BET surface area is 1221 $m^2 g^{-1}$ and the total pore volume is 0.49 $cm^3 g^{-1}$. This high surface area and large pore volume resulted from the known role of KOH as a highly efficient chemical activation agent when combined with a pre-hydrothermal treatment. As shown in **Fig. 1(f)**, the porosity in bare PCS is heavily concentrated in the micropore region with an average pore width of 0.60 nm. Based on the pore size distribution analysis, it is calculated that the volume of microporosity (< 2 mm) is 93.7% of the total pore volume. After the Se impregnation, the surface area dropped significantly, being only 18 $m^2 g^{-1}$ in Se-PCS. This is effectively the geometric surface area of the impregnated carbon nanosheets, as there is negligible porosity available for N_2 adsorption. In turn, this indicates that the available pore surface terminations in PCS are plugged by the selenium phase. This is shown in the BET results in **Fig. 1(e)** as well. The Se fills and closes off the micropores, largely eliminating nitrogen's access to its inner structure. The actual pore size distribution in Se-PCS is shown in **Fig. 1(f)**, further supporting the pores being inaccessible.

Figure 1(g) shows the thermogravimetric analysis (TGA) curve of Se-PCS, indicating that the total mass loading of the Na-active Se phase is 44 wt.%. This is representative of the typical mass loading observed in the battery-materials scientific literature.[42-47] The microstructure of the Se-PCS material was further analyzed by comparing its X-ray diffraction (XRD) pattern to those of as-received monoclinic Se powder and the X-ray amorphous PCS host (**Fig. 1(h)**). The X-ray amorphous structures of both the PCS carbon and the Se agreed with the TEM results. The Se in Se-PCS (middle) is also X-ray amorphous, with a highly broadened reflection centered near $2\theta = 22°$, being associated with short-range ordering in the Se and the amorphous carbon matrix. Likely this broad hump is in fact two separate overlapping highly broadened peaks, one due to short-range ordering in carbon and one due to short-range ordering in Se. High-resolution X-ray photoelectron spectroscopy (XPS) was utilized to investigate the chemical state of the as-synthesized Se in Se-PCS. According to the

XPS survey spectrum shown in **Fig. 1(i)**, the only detectable impurity in Se-PCS is oxygen with a level of 4.3 wt.%. In the high-resolution C1s spectrum (in **Fig. 1(j)**), the dominant peak located at 284.7 eV can be ascribed to the sp2-hybridized carbon with C-C/C=C bands. The peaks situated at 285.8 and 288.1 eV were assigned to C-O and C=O species, respectively. As for the Se 3d spectrum (**Fig. 1(k)**), the peaks located at 55.4 and 56.3 eV were ascribed to the Se 3d 5/2 and 3d 3/2, respectively.

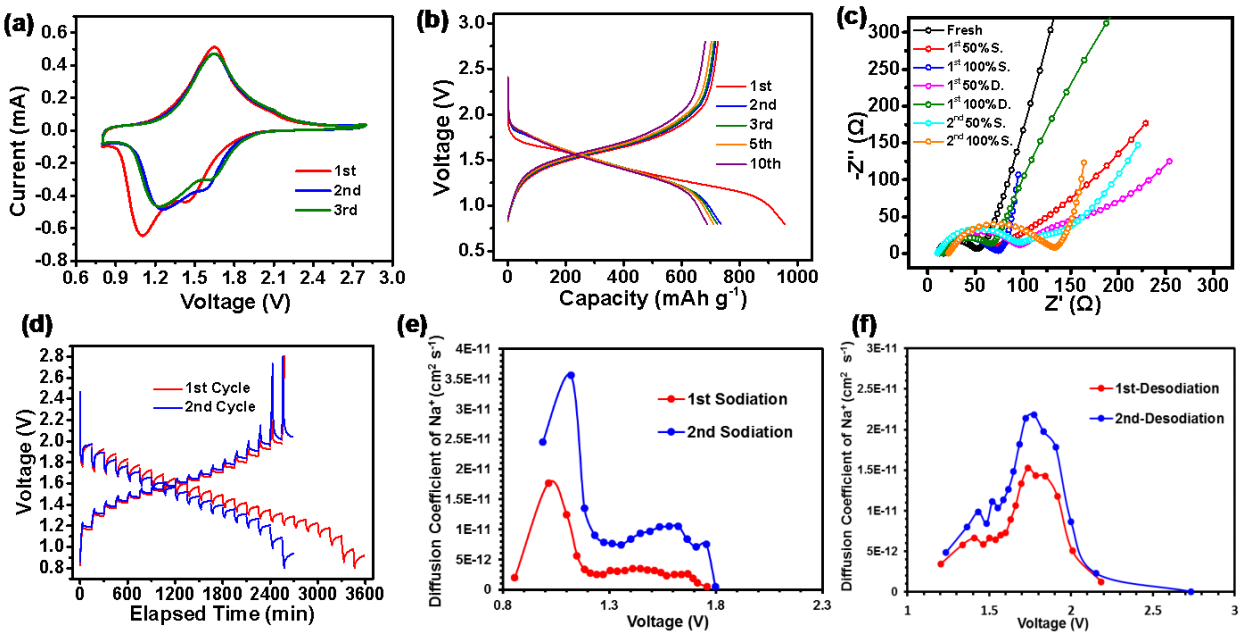

Figure 2. Electrochemical properties of Se-PCS vs. Na/Na^+. (a) CV curves at a scan rate of 0.1 mV s^{-1}. (b) Galvanostatic discharge-charge profiles at 0.1 C (C = 675 mAh g^{-1}, based on the weight of Se). (c) EIS spectra at various charge states at cycle one and two, 50% sodiated, 100% sodiated, 50% desodiated, 100% desodiated. (d) GITT curves of Se-PCS at sodiation-desodiation cycles one and two. A current of 0.05 C was applied for 0.5 h followed by a 2-h relaxation. (e) and (f) Diffusion coefficient of Na^+ calculated from GITT for sodiation and desodiation processes, respectively.

The electrochemical performance of the Se-PCS cathode was investigated in a half-cell configuration, using sodium metal as the anode. A carbonate based electrolyte (1 M $NaClO_4$ in EC:DEC:DMC by a volume ratio of 1:1:1) was employed, without any additives. Cyclic voltammetry (CV), galvanostatic sodiate/desodiate cycling, electrochemical impedance spectroscopy (EIS) and the galvanostatic intermittent titration technique (GITT) were performed to obtain an accurate electroanalytical signature for Se-PCS. For cyclic voltammetry (CV) analysis, the electrodes were tested between 0.8-2.8 V vs. Na/Na^+. **Figure 2(a)** shows the CV curves of Se-PCS at a scan rate of 0.1 mV s^{-1}. In the first scan cycle, there was a pair of cathodic peaks centered at

1.1 and 1.45 V, and a single anodic peak centered at 1.65 V. The peaks on CV represent the redox reaction between selenium and sodium and are clearly asymmetric between sodiation and desodiation. This trend continues at cycles 2 and 3, with two overlapping reduction peaks being present versus what appears to be a broadened but distinctly single oxidation peak. These two peaks shifted towards higher voltage in the following cycles, more significantly for the cathodic peak. The reduction peaks shifted to 1.24 and 1.58 V at cycle 2, and 1.23 and 1.62 V at cycle 3; in all cases the lower voltage reduction peak contributing more to the overall capacity. Similar voltage shifts have been reported by authors in refs.[40, 41] To our knowledge, there have been no conclusive explanations for either the two-peak reduction process or for the shift to more positive reduction voltages with cycle number. A single redox peak pair feature indicates that the electrode undergoes a direct phase change between selenium and Na_2Se without the formation of intermediate species.[48] This is clearly not the case here. In part the shift may be explained by the formation of a solid electrolyte interphase (SEI) in the first cycle below approximately 1 V vs. Na/Na^+. The SEI is known to be catalytically formed at every cycle on fracture surfaces of active materials that are newly exposed to the electrolyte, *e.g.*[49-52] In Se-PCS, the Coulombic efficiency (CE) increased from 76.0 % at the 1st cycle to 97.5 % at the 2nd cycle and to 98.6 % at the 3rd cycle. By cycle 6, the steady-state CE was 100% ± 0.5%, confirming the stability of the initially formed SEI. As will be demonstrated, the differences between sodiation reactions in cycles 1 and 2 are more substantial than just the formation of SEI *per se*.

Figure 2(b) shows the galvanostatic profiles of Se-PCS cathodes at current density of 0.1C (1C equals to 675 mAg^{-1} based on the mass of selenium). Such a slow rate (10 hours to desodiate or sodiate) may be considered to correspond to quasi-equilibrium sodiation. The voltage plateaus in the profile agree relatively well with the peak positions in CV curves, although it is difficult to deconvolve the two cathodic peaks due to their sloping nature. The Se-PCS electrode delivered an initial discharge and charge capacity of 955 mAh g^{-1} and 726 mAh g^{-1}, which are 41.5% and 7.5% greater than the theoretical capacity of Se (675 mAh g^{-1}). The extra and the irreversible portion of cycle 1 discharge capacity is a common behavior in a wide range of Se-carbon cathodes.[18, 39, 53-55] It can be ascribed to a combination of Na storage in PCS (166 mAh g^{-1} per **Fig. S2**) and the formation of SEI by the parasitic reactions of Se with Na^+ as well as the decomposition of electrolyte. In the following desodiation process, PCS

contributed a capacity of 54 mAh g^{-1} (**Fig. S2**), therefore a net capacity of 672 mAh g^{-1} is achieved which is quite close to the theoretical capacity of Se. Although it is not the goal of this study to optimize performance, analysis on a competitive material allows the results to be more applicable to "performance" literature. Achieving close to the theoretical capacity indicates a high level of utilization of the Se and the practical completion of the sodiation reaction.

Electrochemical impedance spectroscopy (EIS) analysis of the Se-PCS cathode was performed in the frequency range of 100 kHz-10 mHz with an amplitude of 10 mV at different sodiate/desodiate states. **Figure 2(c)** depicts these results. The Nyquist plots consist of a semicircle in the high-frequency area and an oblique line in the low-frequency region. After fitting with an equivalent circuit, the simulated data are listed in **Table S1**. The resistance R_s represents the resistance between the electrolyte and the electrode. The single half-circle is termed R_{ct}, and is associated with desodiate-transfer resistance and the contribution from the SEI layer (it was not possible to mathematically separate the two contributions). It may be observed that R_{ct} in the desodiated state is similar before cycling and after the first sodiation-desodiation cycle, being at 40.57 Ω and 57.53 Ω, respectively. In the 100% sodiated state, however, R_{ct} doubles from cycle 1 to cycle 2, going from 52.28 Ω to 101.3 Ω, an effect likely associated with the increased thickness of the SEI layer.

Galvanostatic Intermittent Titration Technique (GITT) analyses of Se-PCS were collected with a 0.5 h current pulse of 0.05 C followed by a 2 h relaxation. These results are shown in **Fig. 2(d)** for sodiation and desodiation, at cycles 1 and 2. The calculated chemical diffusion coefficient of Na^+ ions is shown in **Figs. 2(e)** for sodiation and **2(f)** for desodiation, also at cycles 1 and 2. The diffusion coefficient (D_{Na^+}) values for the sodiation and desodiation processes are in the range of 10^{-10}-10^{-12} cm^2 s^{-1}. Importantly, both the sodiation and the desodiation diffusion constants are significantly higher at cycle 2 than during cycle 1, as is evident from the plots in **Figs. 2(e)-(f)** and data in **Table S2 and S3**.

Comparing the EIS and the GITT findings, it is evident that although the level of SEI increases from cycle 1 to cycle 2, the sodiation-desodiation kinetics are, in fact, more facile. We attribute these results to the irreversible structural changes that occur

in the Se phase going from the as-synthesized microstructure to the microstructure present after the first sodiation cycle. The remaining portion of the manuscript will focus on detailing these complex structural and morphological evolutions. In summary, both TEM and NMR analysis demonstrate that near the conclusion of the first sodiation cycle, there is the creation additional interfaces (*i.e.* cracks) both within the Na-Se and at the Na-Se-carbon interface. This creates a facile route for Na ion diffusion, where the more open structure supports Na ion flux to and from the active Se. Other structural changes that should increase Na ion diffusivity include the irreversible shortening of the Se chains (per NMR) and the elimination of irreversible Na ion trapping, as evidenced by the improved CE at cycle two.

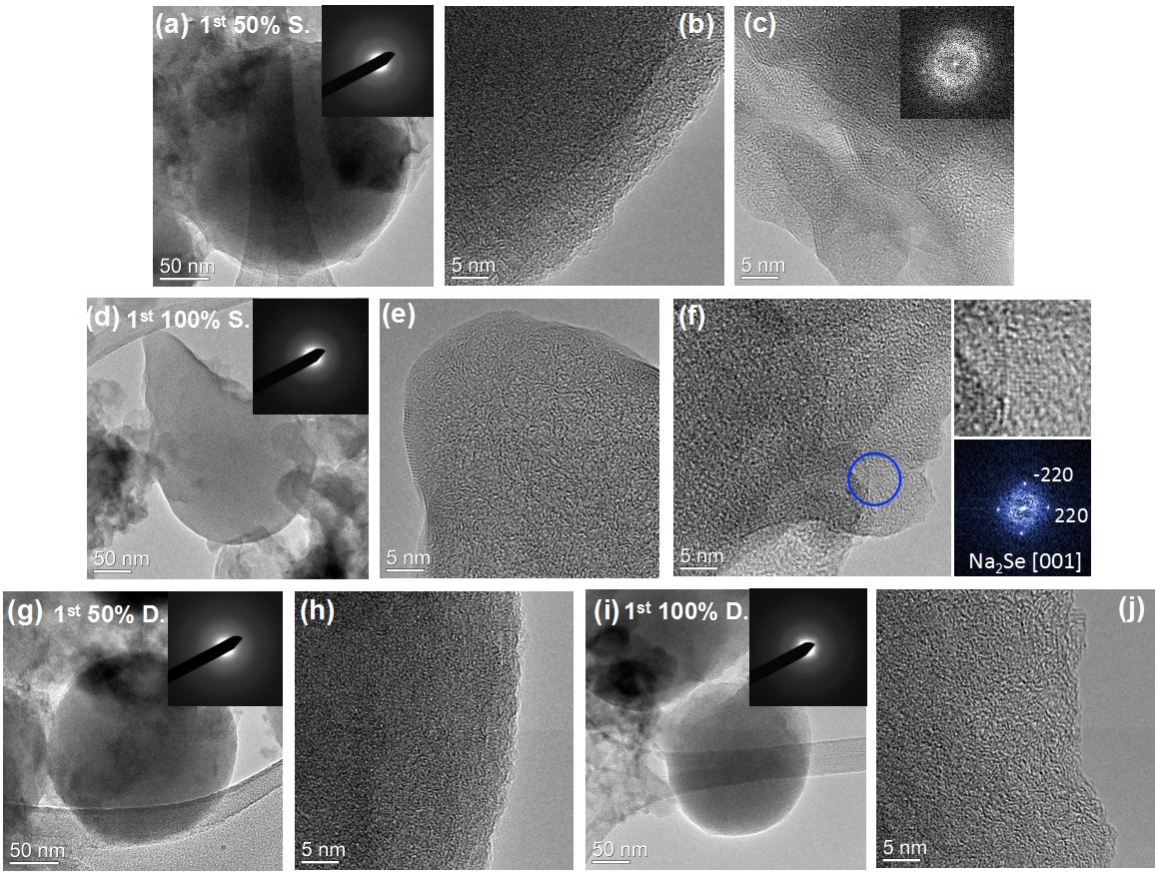

Figure 3. Bright field and high-resolution TEM images with FFT insets. Sample conditions listed are (a)-(c) cycle one, 50% sodiated; (d)-(f) cycle one, 100% sodiated; (g)-(h) cycle one, 50% desodiated; (i)-(j) cycle one, 100% desodiated.

The post-cycled Se-PCS samples were examined by advanced TEM methods, including bright-field (BF) images with the associated selected area electron diffraction (SAED), high-resolution TEM (HRTEM) and electron energy loss spectroscopy (EELS). The BF, SAEDs and HRTEM analyses are shown in **Figs. 3** and **4**, while the

EELS results are shown in **Fig. 5**. Extreme care was taken during TEM analysis not to create beam-induced artifacts, for example by keeping the electron dose below 15 pA cm^{-2} on the fluorescent screen for analyzed regions, and by performing focus operations not directly on the region of interest. According to **Fig. 3**, at cycle one and 50% sodiation, the vast majority of the Se is fully amorphous. This is supported by the SAED associated with the BF image. A minority of the Se is nanocrystalline, however, as evidenced by the HRTEM image in **Fig. 3(c)**. In the associated Fast Fourier Transform (FFT) inset, the ring spacing correlates with the equilibrium Na_2Se_2 crystal structure.[56] The crystallites were too fine to index individually. According to **Figs. 3(d)** and **3(e)**, the majority of the terminally sodiated Se structure is fully amorphous. However, as shown in **Fig. 3(f)**, there are some isolated Na_2Se crystallites present. The Na_2Se crystallites were indexed as equilibrium *fcc* structure.[57] Per **Figs. 3(g)-(j)**, the first-cycle 50% desodiated and 100% desodiated Se are fully amorphous. There was no evidence of localized crystallization.

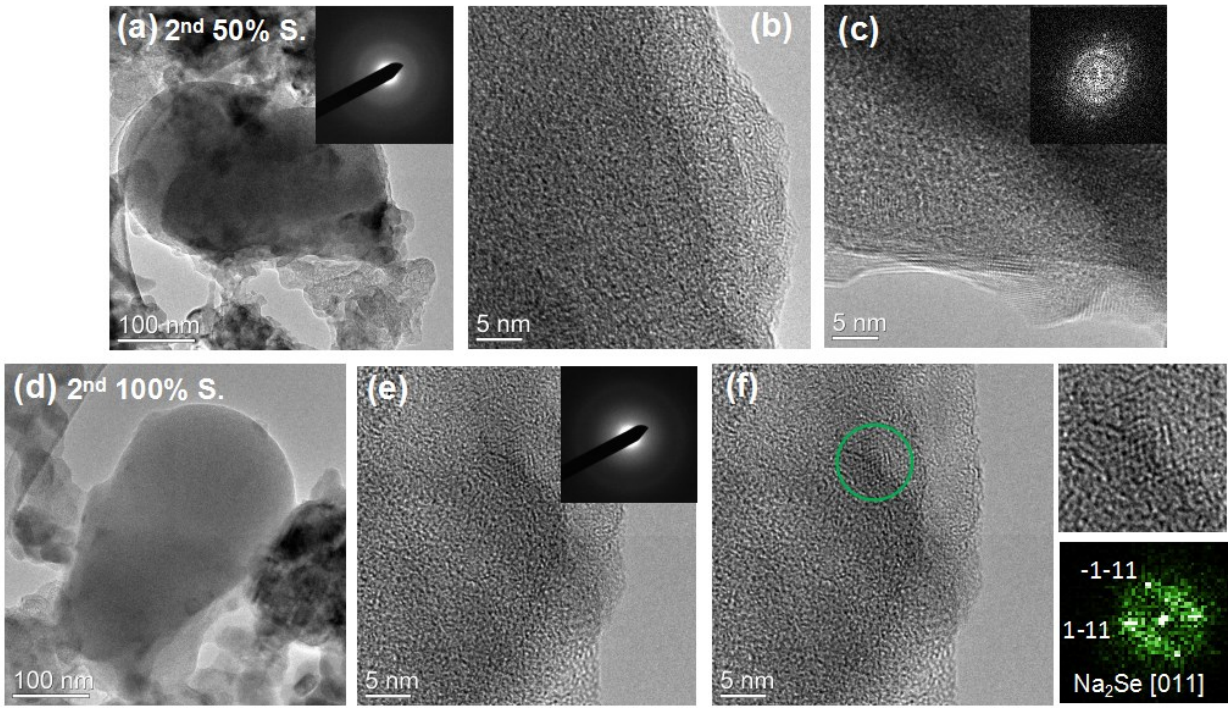

Figure 4. Bright-field and high-resolution TEM images with FFT insets. Sample conditions listed are (a)-(c) cycle two, 50% sodiated; (d)-(f) cycle two, 100% sodiated.

A similar reaction sequence and microstructure was observed during the second sodiation cycle. These results are shown in **Figs. 4(a)-(f)**. The majority of the Se structure is amorphous at 50% and 100% sodiation. There are again localized regions at 50% and 100% sodiation that are nanocrystalline form of the equilibrium structures.

It was not possible to ascertain the relative fraction of the crystallized regions at cycle one versus at cycle two. It should be noted that extreme care was also used to ensure that oxidation-induced artifacts did not affect the analysis. To understand the role of air exposure, a separate sample was purposely oxidized prior to analysis. It was sodiated to the terminal voltage of 0.8 V vs. Na/Na^+. The electrode was disassembled inside a glove box and a standard TEM specimen was fabricated from it. The TEM specimen, however, was held for 3 hours in air prior to analysis. These STEM analysis results are given in **Fig. S3**. There appears to be a distinct oxidized structure that consists of rods of Na-rich material (likely Na_2O and/or NaOH) actually extruding from the specimen as isolated particles and laths. This morphology is distinct from what is present in **Figs. 3-5** and **S4-S6.**

The changes in electrode morphology and in the Se-Na bonding were investigated with high-angle annular dark-field scanning transmission electron microscopy (HAADF-STEM) and STEM-EELS. The Se and Na-Se phases are much denser than the carbon host, and therefore appear brighter in HAADF images due to their mass-thickness contrast. **Figure 5(a)** shows a series of HAADF images highlighting the evolution of the electrodes with different states of charge. Per **Figs. 5(b)** and **(c)** the Na K-edge showed clear changes after sodiation or desodiation: the Na K-edge was observed at 50% and 100% sodiated samples while it disappeared in the 50% and 100% desodiated samples. According to **Fig. 5(a)**, the sodiation process changes the morphology of the Se from entirely spherical to a combination of spherical and blocky regions. The most extreme changes are in the 100% sodiated specimens, both at the first and at the second sodiation cycle. It is expected that the amorphous portions of the Na-Se compounds (Na_2Se, Na_2Se_2) should not adopt an anisotropic morphology. There is direct evidence of nanoscale cracking-pulverization within the Se-Na phases, which would be expected due the severe volume changes upon sodiation. This can be qualitatively understood by considering the density changes from Se (4.81 g cm^{-3}) to Na_2Se_2 (3.25 g cm^{-3}) and Na_2Se (2.62 g cm^{-3}). Therefore, the blocky portions of the microstructure likely originate from the electrode material being fractured. In addition, some angularity may originate from the minority nanocrystallites.

It is unlikely that during sodiation, the carbon host dynamically changes its morphology to accommodate the Se reaction. Sodiation-induced shape changes have

not been reported for amorphous carbons.[13, 58] Therefore, one can conclude that sodiation will also create geometric misfit between the two materials, *i.e.* localized nanoscale gaps between the active Se phase and its carbon host. This scenario will be confirmed by NMR. The additional interface area introduced near the first terminal sodiation helps to explain the profound changes in the electrochemical reaction kinetics and in the Na ion diffusivity. Examining the 100% desodiated specimens at cycle one and two, it is evident that the Se phase reverts to its spherical morphology. It is also evident that the electrode fracturing becomes less pronounced, suggesting a self-healing mechanism that needs further study. The possible dynamic healing aspect of the desodiation reaction needs to be understood further, although a similar phenomenon has been observed by *in-situ* TEM for desodiation of SnSb.[59] One would not expect the carbon host to self-heal were it to fracture, since its structure is static rather than dynamic with state of charge. The described sodiation-induced changes in the morphology and the cracking are confirmed with a number of additional examples. Those results are shown in **Figs. S4-S6**.

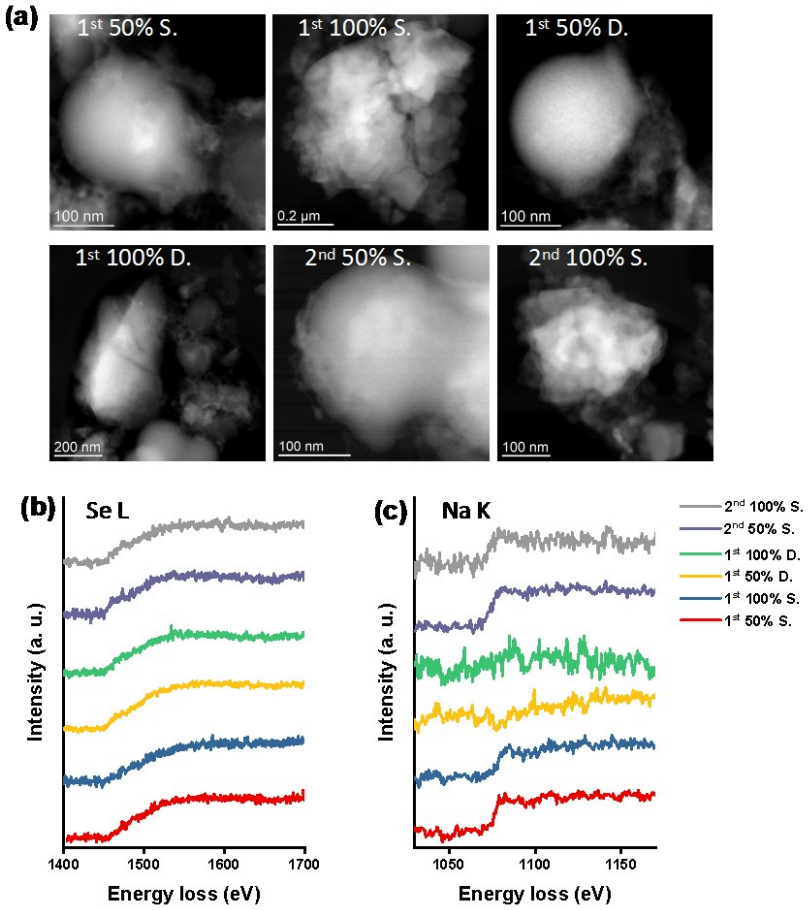

Figure 5. (a) HAADF-STEM images of Se-PCS samples at different states of charge. STEM-EELS of (b) Se L-edge and (c) Na K-edge of Se-PCS samples.

Table 1. Expected ^{77}Se chemical shifts for the relevant selenium species.

Compounds	δ(^{77}Se) / ppm[a]
Se^{2-}	-720[b]
Se_2^{2-}	-415[c]
Se_3^{2-}	193 (α), 214 (β)
Se_4^{2-}	256 (α), 581 (β)
Se_5^{2-}	354 (α), 570 (β), 868 (γ)
Se_8	670
Se_∞	900
SeO_4^{2-}	1040

[a]Most shifts are taken from ref 27. [b]Experimentally determined in this work. [c]The Se_2^{2-} ion has not been observed by ^{77}Se SSNMR, as it is unstable in solution.[27] This value was extrapolated using the ^{125}Te chemical shift of Te_2^{2-} (-1080 ppm) and the ^{77}Se and ^{125}Te chemical shifts of the Ch^{2-}, Ch_3^{2-}, Ch_4^{2-} anions[26] and those for elemental Se[28] and Te.[60, 61] The relationship is $\delta(^{77}Se) = 0.8519 \cdot \delta(^{129}Te) + 500.23$ ppm, $R^2 = 0.9948$; with both values referenced to $Ch(Me)_2$.

To obtain further insight into the local structure, ^{77}Se solid-state nuclear magnetic resonance spectroscopy (SSNMR) spectroscopy was performed. The specimens analyzed with SSNMR were identical to the ones studied by electroanalytical methods and TEM. The various polyselenides, of the form Na_2Se_n (i.e., Se_n^{2-} ions) can be identified by the technique (see **Table 1**).[26-35] This provides a chemical handle on the evolving composition of the cathode. The ^{77}Se chemical shift steadily decreases as selenium is reduced from the maximum values of 900 and 670 for elemental Se_∞ and Se_8, respectively,[34] down to -720 ppm for the mono-selenide ion.[27] It is worth noting that, in earlier studies, ^{17}O and ^{33}S SSNMR have also been applied to the identification of the discharge products in Li-S[62] and Li-O_2[63] batteries.

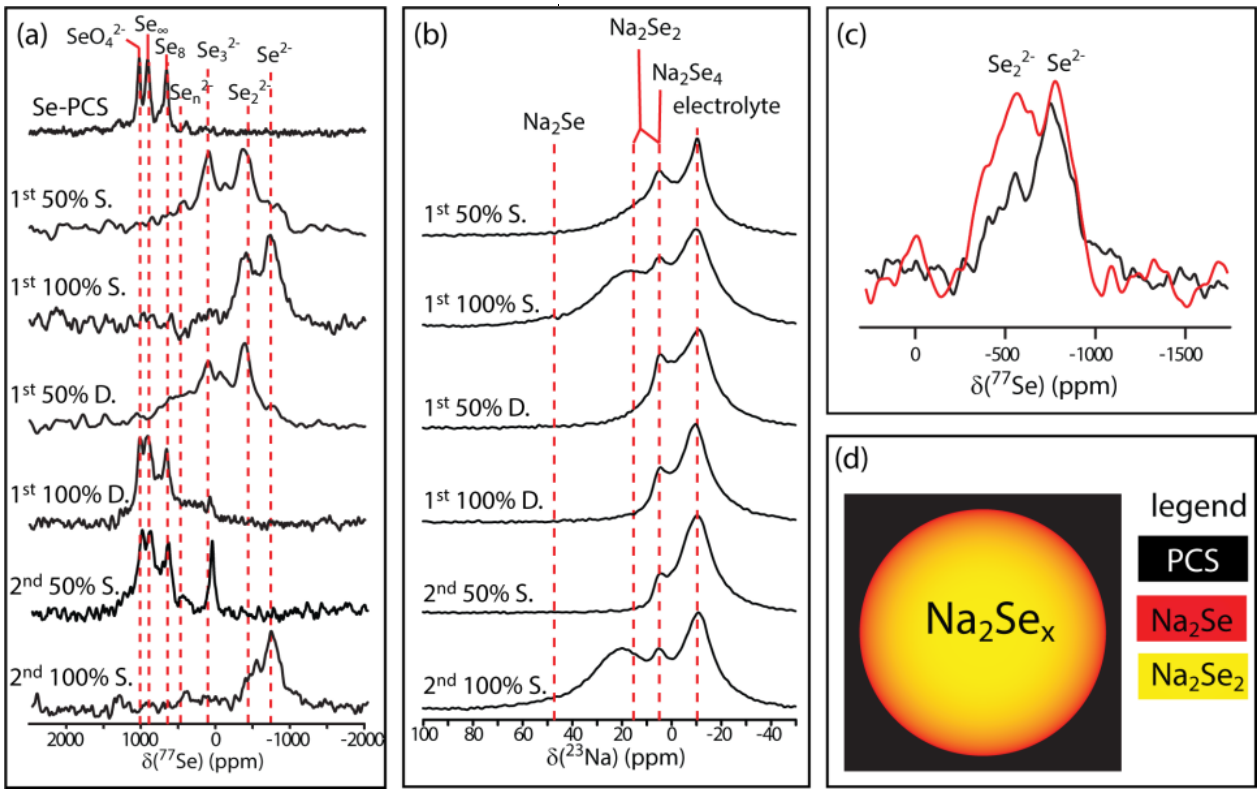

Figure 6. (a) Se MAS SSNMR spectra; dashed red lines are the expected chemical shifts for the various polyselenides, per Figure S1 and Table S1. (b) ^{23}Na MAS SSNMR spectra; dashed lines highlight the positions of the expected sharp resonances from crystalline polyselenides, as well as the electrolyte. (c) ^{77}Se MAS SSNMR spectra acquired for the second cycle; a 100% sodiated, sample using recycle delays of 0.5 s (black) and 60 s (red). (d) A schematic representation of the obtained local chemistry of a sodiated Se particle confined inside a carbon micropore.

The ^{77}Se MAS SSNMR spectra of the Se-PCS samples are shown in **Fig. 6(a)**. The as-synthesized Se-PCS material features nearly equally intense resonances from the linear and cyclical selenium (Se_8), along with a resonance from oxidized selenium (selenate).[64] As the Se-PCS becomes sodiated, there is a complete disappearance of these three species and the appearance of new resonances at a lower frequency originating from the polyselenides. As the Se-PCS electrode is cycled, the spectral intensity oscillates between the high- and low-frequency extrema of the spectrum. In contrast to the mechanisms that have been elucidated for some Li/Se batteries[18], there is no evidence for there being discrete phase transitions as the material is sodiated. Rather, there is progressive shortening of the polyselenide chains as selenium is reduced; mono-, di-, and tri-selenides, as well as longer ions, are all detected simultaneously in a given material (for example the first cycle, 50% sodiated sample). This is also the first evidence for the presence of Se_3^{2-} ions during the discharge. In the fully sodiated Se-

PCS there is the formation of both Na_2Se_2 and Na_2Se, with the longer chains now having been reduced.

At cycle two, the fully desodiated Se-PCS (1st 100% D.) yields a ^{77}Se MAS SSNMR spectrum that is similar to that of the as-synthesized material. However, there is one important difference: There is noticeable intensity at lower frequency, corresponding to Se_3^{2-} as well as some longer polyselenides ions. This indicates that some of the polyselenide ions were unsuccessfully desodiated, perhaps due to a loss of good electrical contact with the carbon. As this material is sodiated for the second time, it is these species Se_n^{2-} that are first reduced anew to form, predominantly, Se_3^{2-} at the 50% sodiation point. Unlike the first cycle, the reduction was anisotropic. There was significant amount of elemental Se at the 50% mark, while there was none at the first cycle. The fully sodiated sample from this second cycle is again composed of Na_2Se and Na_2Se_2. However, the observed fraction of the signal originating from the fully reduced Na_2Se is greater than that observed in the first cycle. This agrees well with the GITT derived Na^+ diffusivity findings, *i.e.* the faster Na^+ diffusivity promotes easier sodiation to the equilibrium phase.

The sodiation-desodiation process was further analyzed by observing ^{23}Na. Due to a lack of available experimental ^{23}Na SSNMR data for the pure sodium polyselenides, the ^{23}Na SSNMR spectra was predicted using GIPAW DFT calculations. GIPAW DFT is known for its accuracy in reproducing electric field gradient and chemical shift tensors for solids.[65, 66] In particular, the accuracy in PAW DFT calculations of ^{23}Na electric field gradient tensors has been leveraged for NMR-based crystallographic structure refinements of powder structures.[67, 68] The calculated ^{23}Na quadrupolar coupling parameters and chemical shifts are listed in **Table S4**, while the simulated spectra are shown in **Fig. S7**. At the field of 9.4 T, the Na_2Se_3 and Na_2Se_5 species are difficult to observe due to their resonances either overlapping with that from the free electrolyte [36], or being far broader due to a stronger quadrupolar coupling. The other three sodium selenides, however, feature sharp resonances that are readily detected if nanocrystalline domains are formed.[69] The ^{23}Na MAS SSNMR spectra of all sodiated samples are shown in **Fig. 6(b)**. Per the figure, there is evidence of the formation of crystalline Na_2Se, which has been analyzed in its pure form as baseline (**Fig. S8**).

To understand the differences observed by ^{77}Se and ^{23}Na SSNMR spectroscopies it should be noted that that the ^{77}Se SSNMR spectra are T_1-weighted, whereas the ^{23}Na spectra are not. It is well-known that ^{77}Se T_1 relaxation times are very long,[32] as with most spin-1/2 nuclei. It was observed experimentally that the optimal relaxation delay to acquire the spectra on the cathode materials was 0.5 s. This is in stark contrast with the pure Na_2Se for which a relaxation delay of 2 hours was required to detect the ^{77}Se SSNMR signal. It is evident that the ^{77}Se relaxation is enhanced by the carbon support. Given that pyrolyzed carbon materials are known to being paramagnetic,[70, 71] the likely cause of the accelerated relaxation in the carbon materials is paramagnetic relaxation enhancement (PRE).[72] Given that PREs depend on the inverse sixth power of the electron-nuclear distance,[72] it follows that the ^{77}Se must be weighted towards the preferential detection of Se sites near the Se/C interface. It is noted that the ^{23}Na spectra were acquired with delays that assured quantitative accuracy. While ^{23}Na SSNMR detects all nuclei in the reduced Se-PCS material, the ^{77}Se SSNMR favors the selenide species situated at the Se/C interface. To confirm, the ^{77}Se MAS SSNMR spectrum on the second cycle 100% sodiated sample was acquired using a considerably longer relaxation delay of 60 s. This spectrum is shown in **Fig. 6(c)**. The figure demonstrates that the Na_2Se_2 fraction of the spectrum grows with respect to the spectrum acquired with a recycle delay of 0.5 s. It can then be concluded that the fully reduced Na_2Se fraction is situated exclusively at the Se/C interface, with the less reduced Na_2Se_2 regions being in the center.

The ^{77}Se SSNMR spectra are weighted in favor of the detection of Se sites situated at the interface with the carbon support. This allows for further mechanistic insight from the data shown in **Fig. 6(d)**. Comparing the spectra for the first cycle 50% (de)sodiated samples, it is evident that sample being sodiated has its intensity weighted towards a lower frequency (*i.e.* more reduced) than the sample being desodiated. This data further supports the conclusion that the more reduced Na_2Se is found at the interface. The reduction and oxidation reactions first take place at the C-Se interface, with the reaction front moving inward toward the core. The difference in the densities, *i.e.* the associated volume expansion, of the two phases Na_2Se_2 (3.25 g cm^{-3}) and Na_2Se (2.62 g cm^{-3}) creates large strain heterogeneities in the active material. A spatially heterogenous sodiation sequence would help to explain the observed sodiation-induced fracture.

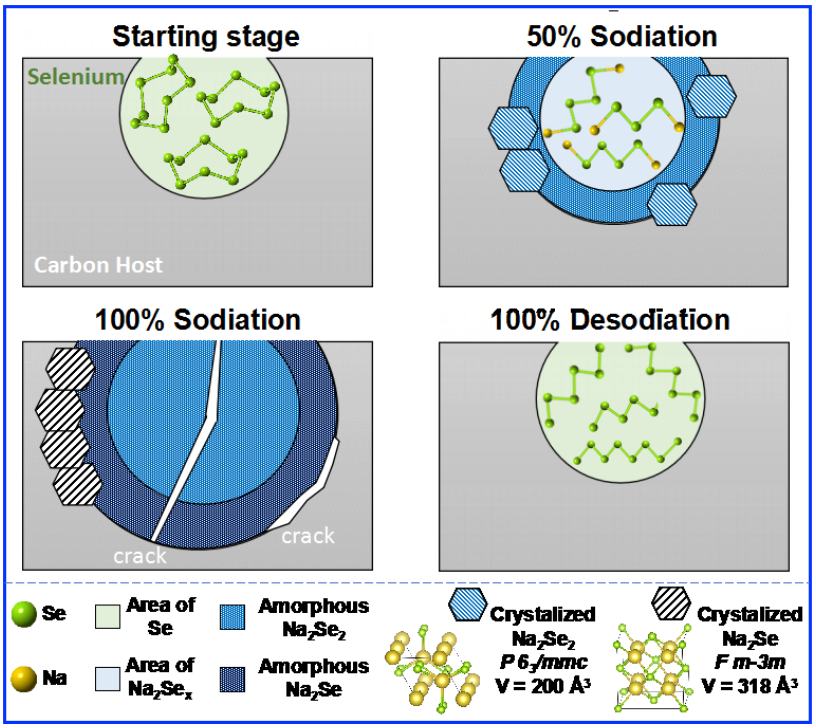

Scheme 1. Summary of the key aspects of phase transformation sequence during sodiation and desodiation of Se-PCS.

Scheme 1 summarizes the key observations regarding the sodiation-desodiation sequence of Se-PCS. During first sodiation, the Se chains are progressively cut to form an amorphous mixture of polyselenides of varying lengths. The Se nearest the carbon pore surface is sodiated first, leading to the formation of a core-shell compositional profile. There is no evidence for a sequence of discrete phase transitions between Na_2Se_4, Na_2Se_2, and Na_2Se. At 50% and 100% sodiation, the majority of Se-Na is amorphous, with minority nanocrystalline Na_2Se_2 (hcp) or Na_2Se (fcc) equilibrium phases. Near 100% sodiation, the Se phase evolves from spherical to mixed spherical-blocky, and then back to spherical upon 100% desodiation. Nanoscale pulverization of terminally sodiated Na-Se is observed, with some evidence of self-healing at subsequent desodiation. The initial versus the second sodiations also show key differences: There is physical separation of some Se from the carbon host after the first cycle and a threefold increase in Na^+ diffusivity at cycle two. The overall sodiation-desodiation sequence in these pore-confined Se structures appears more complex than the transformations described in literature for unconfined nanoscale Se.

ASSOCIATED CONTENT

The Supporting Information is available free of charge on the ACS Publications website at DOI:

Detailed experimental procedures, additional SEM, STEM, NMR, EIS and electrochemical results (PDF)

AUTHOR INFORMATION

Corresponding Authors

*Email: *fperras@ameslab.gov.*

*Email: *David.Mitlin@austin.utexas.edu.*

Author Contributions

All authors have given approval to the final version of the manuscript.

Notes

The authors declare no competing financial interest.

ACKNOWLEDGMENT

F.P., M.P. (NMR research, manuscript preparation), and R.B. (DFT calculations) were supported by the U.S. Department of Energy (DOE), Office of Science, Basic Energy Sciences, Materials Science and Engineering Division at the Ames Laboratory. The Ames Laboratory is operated for the DOE by Iowa State University under Contract No. DE-AC02-07CH11358. D.M. (research conception and guidance, manuscript preparation), VH-P, Y.W., P.L. (synthesis, electrochemical analysis) were supported by the U.S. Department of Energy, Office of Basic Energy Sciences, Division of Materials Sciences and Engineering under Award # DE-SC0018074. Electron microscopy work (S.H. and D.S.) was performed at the Center for Functional Nanomaterials, which is a U.S. DOE Office of Science Facility, at Brookhaven National Laboratory under Contract No. DE-SC0012704. E.S. and J.N. (TEM specimen preparation) were sponsored by Energy Storage Program, Office of Electricity, Department of Energy, USA.

REFERENCES

(1) Manthiram, A.; Fu, Y.; Chung, S.-H.; Zu, C.; Su, Y.-S. Rechargeable lithium–sulfur batteries. *Chem. Rev.* **2014**, 114, 11751-11787.

(2) Rozier, P.; Tarascon, J. M. Li-rich layered oxide cathodes for next-generation Li-ion batteries: chances and challenges. *J. Electrochem. Soc.* **2015**, 162, A2490-A2499.
(3) Pu, J.; Li, J.; Shen, Z.; Zhong, C.; Liu, J.; Ma, H.; Zhu, J.; Zhang, H.; Braun, P. V. Interlayer Lithium Plating in Au Nanoparticles Pillared Reduced Graphene Oxide for Lithium Metal Anodes. *Adv. Funct. Mater.* **2018**, 28.
(4) Abouimrane, A.; Dambournet, D.; Chapman, K. W.; Chupas, P. J.; Weng, W.; Amine, K. A new class of lithium and sodium rechargeable batteries based on selenium and selenium-sulfur as a positive electrode. *J. Am. Chem. Soc.* **2012**, 134, 4505-4508.
(5) Lee, B.; Paek, E.; Mitlin, D.; Lee, S. W. Sodium Metal Anodes: Emerging Solutions to Dendrite Growth. *Chem. Rev.* **2019**, 119, 5416-5460.
(6) Liu, W.; Li, P.; Wang, W.; Zhu, D.; Chen, Y.; Pen, S.; Paek, E.; Mitlin, D. Directional Flow-Aided Sonochemistry Yields Graphene with Tunable Defects to Provide Fundamental Insight on Sodium Metal Plating Behavior. *ACS Nano* **2018**, 12, 12255-12268.
(7) Yu, X.; Manthiram, A. Ambient‐Temperature Sodium–Sulfur Batteries with a Sodiated Nafion Membrane and a Carbon Nanofiber‐Activated Carbon Composite Electrode. *Adv. Energy Mater.* **2015**, 5, 1500350.
(8) Wang, Y.-X.; Yang, J.; Lai, W.; Chou, S.-L.; Gu, Q.-F.; Liu, H. K.; Zhao, D.; Dou, S. X. Achieving high-performance room-temperature sodium–sulfur batteries with S@ interconnected mesoporous carbon hollow nanospheres. *J. Am. Chem. Soc.* **2016**, 138, 16576-16579.
(9) Manthiram, A.; Yu, X. Ambient temperature sodium–sulfur batteries. *Small* **2015**, 11, 2108-2114.
(10) Xin, S.; Yin, Y. X.; Guo, Y. G.; Wan, L. J. A high‐energy room‐temperature sodium‐sulfur battery. *Adv. Mater.* **2014**, 26, 1261-1265.
(11) Greenwood, N. N.; Earnshaw, A., *Chemistry of the Elements*. Elsevier: 2012.
(12) Kotkata, M.; Kandil, K. A study of the electrical conductivity of amorphous-crystalline selenium mixtures. *Mater. Sci. Eng.* **1987**, 95, 287-293.
(13) Lee, B.; Paek, E.; Mitlin, D.; Lee, S. W. Sodium Metal Anodes: Emerging Solutions to Dendrite Growth. *Chem. Rev.* **2019**, 119, 5416-5460.
(14) Cui, Y.; Abouimrane, A.; Lu, J.; Bolin, T.; Ren, Y.; Weng, W.; Sun, C.; Maroni, V. A.; Heald, S. M.; Amine, K. (De)lithiation mechanism of Li/SeS(x) (x = 0-7)

batteries determined by in situ synchrotron X-ray diffraction and X-ray absorption spectroscopy. *J. Am. Chem. Soc.* **2013**, 135, 8047-8056.

(15) Li, Z.; Zhang, J.; Lu, Y.; Lou, X. W. D. A pyrolyzed polyacrylonitrile/selenium disulfide composite cathode with remarkable lithium and sodium storage performances. *Sci. Adv.* **2018**, 4, eaat1687.

(16) Pham, V. H.; Boscoboinik, J. A.; Stacchiola, D. J.; Self, E. C.; Manikandan, P.; Nagarajan, S.; Wang, Y.; Pol, V. G.; Nanda, J.; Paek, E.; Mitlin, D. Selenium-sulfur (SeS) fast charging cathode for sodium and lithium metal batteries. *Energy Storage Mater.* **2019**, 20, 71-79.

(17) Li, Q.; Liu, H.; Yao, Z.; Cheng, J.; Li, T.; Li, Y.; Wolverton, C.; Wu, J.; Dravid, V. P. Electrochemistry of selenium with sodium and lithium: kinetics and reaction mechanism. *ACS Nano* **2016**, 10, 8788-8795.

(18) Xin, S.; Yu, L.; You, Y.; Cong, H.-P.; Yin, Y.-X.; Du, X.-L.; Guo, Y.-G.; Yu, S.-H.; Cui, Y.; Goodenough, J. B. The electrochemistry with lithium versus sodium of selenium confined to slit micropores in carbon. *Nano Lett.* **2016**, 16, 4560-4568.

(19) Zeng, L.; Zeng, W.; Jiang, Y.; Wei, X.; Li, W.; Yang, C.; Zhu, Y.; Yu, Y. A Flexible Porous Carbon Nanofibers‐Selenium Cathode with Superior Electrochemical Performance for Both Li‐Se and Na‐Se Batteries. *Adv. Energy Mater.* **2015**, 5, 1401377.

(20) Zeng, L.; Wei, X.; Wang, J.; Jiang, Y.; Li, W.; Yu, Y. Flexible one-dimensional carbon–selenium composite nanofibers with superior electrochemical performance for Li–Se/Na–Se batteries. *J. Power Sources* **2015**, 281, 461-469.

(21) Wang, H.; Li, S.; Chen, Z.; Liu, H. K.; Guo, Z. A novel type of one-dimensional organic selenium-containing fiber with superior performance for lithium–selenium and sodium–selenium batteries. *RSC Adv.* **2014**, 4, 61673-61678.

(22) He, K.; Zhou, Y.; Gao, P.; Wang, L.; Pereira, N.; Amatucci, G. G.; Nam, K.-W.; Yang, X.-Q.; Zhu, Y.; Wang, F. Sodiation via heterogeneous disproportionation in FeF2 electrodes for sodium-ion batteries. *ACS Nano* **2014**, 8, 7251-7259.

(23) Wang, Y.; Mu, L.; Liu, J.; Yang, Z.; Yu, X.; Gu, L.; Hu, Y. S.; Li, H.; Yang, X. Q.; Chen, L. A Novel High Capacity Positive Electrode Material with Tunnel‐Type Structure for Aqueous Sodium‐Ion Batteries. *Adv. Energy Mater.* **2015**, 5, 1501005.

(24) Wang, C.-M. In situ transmission electron microscopy and spectroscopy studies of rechargeable batteries under dynamic operating conditions: A retrospective and perspective view. *J. Mater. Res.* **2015**, 30, 326-339.
(25) McDowell, M. T.; Ryu, I.; Lee, S. W.; Wang, C.; Nix, W. D.; Cui, Y. Studying the kinetics of crystalline silicon nanoparticle lithiation with in situ transmission electron microscopy. *Adv. Mater.* **2012**, 24, 6034-6041.
(26) Björgvinsson, M.; Schrobilgen, G. Homo-and heteropolychalcogenide anions Ch 2-, HCh-, Ch 2 2-, Ch 3 2-, Ch 3 2-, and Ch 4 2-(Ch= Se and/or Te): Solution 1 H, 77 Se, 123 Te, and 125 Te NMR study. *Inorg. Chem.* **1991**, 30, 2540-2547.
(27) Cusick, J.; Dance, I. The characterization of [HSe]− and [Sex] 2− ions by 77Se NMR. *Polyhedron* **1991**, 10, 2629-2640.
(28) Chivers, T.; Laitinen, R. S.; Schmidt, K. J. 77Se NMR spectroscopic study of the molecular composition of sulfur–selenium melts. *Can. J. Chem.* **1992**, 70, 719-725.
(29) Barrie, P. J.; Clark, R. J.; Chung, D.-Y.; Chakrabarty, D.; Kanatzidis, M. G. 77Se Solid-State NMR Spectroscopy and Structures of Tetramethylammonium Pentaselenide and Hexaselenide Complexes. *Inorg. Chem.* **1995**, 34, 4299-4304.
(30) Duddeck, H. Selenium-77 nuclear magnetic resonance spectroscopy. *Prog. Nucl. Magn. Reson. Spectrosc.* **1995**, 27, 1-323.
(31) Demko, B. A.; Wasylishen, R. E. Solid-state selenium-77 NMR. *Prog. Nucl. Magn. Reson. Spectrosc.* **2009**, 3, 208-238.
(32) Sen, S.; Kaseman, D. C.; Hung, I.; Gan, Z. 77se nuclear spin–lattice relaxation in binary ge–se glasses: Insights into floppy versus rigid behavior of structural units. *J. Phys. Chem. B* **2015**, 119, 5747-5753.
(33) Kaseman, D. C.; Oliveira, K. M.; Palazzo, T.; Sen, S. Selenium Chain Length Distribution in Ge x Se100–x Glasses: Insights from 77Se NMR Spectroscopy and Quantum Chemical Calculations. *J. Phys. Chem. B* **2016**, 120, 4513-4521.
(34) Marple, M.; Badger, J.; Hung, I.; Gan, Z.; Kovnir, K.; Sen, S. Structure of amorphous selenium by 2D 77Se NMR spectroscopy: an end to the dilemma of chain versus ring. *Angew. Chem. Int. Ed.* **2017**, 56, 9777-9781.
(35) Yuan, B.; Zhu, W.; Hung, I.; Gan, Z.; Aitken, B.; Sen, S. Structure and Chemical Order in S–Se Binary Glasses. *J. Phys. Chem. B* **2018**, 122, 12219-12226.
(36) Koller, H.; Engelhardt, G.; Kentgens, A. P.; Sauer, J. 23Na NMR spectroscopy of solids: Interpretation of quadrupole interaction parameters and chemical shifts. *J. Phys. Chem. B* **1994**, 98, 1544-1551.

(37) Mali, G.; Patel, M. U.; Mazaj, M.; Dominko, R. Stable Crystalline Forms of Na Polysulfides: Experiment versus Ab Initio Computational Prediction. *Chem. Eur. J.* **2016**, 22, 3355-3360.

(38) See, K. A.; Leskes, M.; Griffin, J. M.; Britto, S.; Matthews, P. D.; Emly, A.; Van der Ven, A.; Wright, D. S.; Morris, A. J.; Grey, C. P. Ab initio structure search and in situ 7Li NMR studies of discharge products in the Li–S battery system. *J. Am. Chem. Soc.* **2014**, 136, 16368-16377.

(39) Li, Z.; Yuan, L.; Yi, Z.; Liu, Y.; Huang, Y. Confined selenium within porous carbon nanospheres as cathode for advanced Li–Se batteries. *Nano Energy* **2014**, 9, 229-236.

(40) Luo, C.; Xu, Y.; Zhu, Y.; Liu, Y.; Zheng, S.; Liu, Y.; Langrock, A.; Wang, C. Selenium@ mesoporous carbon composite with superior lithium and sodium storage capacity. *ACS Nano* **2013**, 7, 8003-8010.

(41) Ding, J.; Zhou, H.; Zhang, H.; Stephenson, T.; Li, Z.; Karpuzov, D.; Mitlin, D. Exceptional energy and new insight with a sodium–selenium battery based on a carbon nanosheet cathode and a pseudographite anode. *Energy Environ. Sci.* **2017**, 10, 153-165.

(42) Yang, J.; Gao, H.; Ma, D.; Zou, J.; Lin, Z.; Kang, X.; Chen, S. High-performance Li-Se battery cathode based on CoSe2-porous carbon composites. *Electrochim. Acta* **2018**, 264, 341-349.

(43) Zeng, L.; Chen, X.; Liu, R.; Lin, L.; Zheng, C.; Xu, L.; Luo, F.; Qian, Q.; Chen, Q.; Wei, M. Green synthesis of a Se/HPCF–rGO composite for Li–Se batteries with excellent long-term cycling performance. *J. Mater. Chem. A* **2017**, 5, 22997-23005.

(44) Zhang, J.; Fan, L.; Zhu, Y.; Xu, Y.; Liang, J.; Wei, D.; Qian, Y. Selenium/interconnected porous hollow carbon bubbles composites as the cathodes of Li–Se batteries with high performance. *Nanoscale* **2014**, 6, 12952-12957.

(45) Yang, C. P.; Xin, S.; Yin, Y. X.; Ye, H.; Zhang, J.; Guo, Y. G. An advanced selenium–carbon cathode for rechargeable lithium–selenium batteries. *Angew. Chem. Int. Ed.* **2013**, 52, 8363-8367.

(46) Liu, T.; Zhang, Y.; Hou, J.; Lu, S.; Jiang, J.; Xu, M. High performance mesoporous C@Se composite cathodes derived from Ni-based MOFs for Li–Se batteries. *RSC Adv.* **2015**, 5, 84038-84043.

(47) Jiang, Y.; Ma, X.; Feng, J.; Xiong, S. Selenium in nitrogen-doped microporous carbon spheres for high-performance lithium–selenium batteries. *J. Mater. Chem. A* **2015**, 3, 4539-4546.

(48) Cui, Y.; Abouimrane, A.; Lu, J.; Bolin, T.; Ren, Y.; Weng, W.; Sun, C.; Maroni, V. A.; Heald, S. M.; Amine, K. (De) Lithiation mechanism of Li/SeS x (x= 0–7) batteries determined by in situ synchrotron X-ray diffraction and X-ray absorption spectroscopy. *J. Am. Chem. Soc.* **2013**, 135, 8047-8056.

(49) Lotfabad, E. M.; Kalisvaart, P.; Kohandehghan, A.; Cui, K.; Kupsta, M.; Farbod, B.; Mitlin, D. Si nanotubes ALD coated with TiO 2, TiN or Al 2 O 3 as high performance lithium ion battery anodes. *J. Mater. Chem. A* **2014**, 2, 2504-2516.

(50) Kohandehghan, A.; Kalisvaart, P.; Cui, K.; Kupsta, M.; Memarzadeh, E.; Mitlin, D. Silicon nanowire lithium-ion battery anodes with ALD deposited TiN coatings demonstrate a major improvement in cycling performance. *J. Mater. Chem. A* **2013**, 1, 12850-12861.

(51) Kohandehghan, A.; Kalisvaart, P.; Kupsta, M.; Zahiri, B.; Amirkhiz, B. S.; Li, Z.; Memarzadeh, E. L.; Bendersky, L. A.; Mitlin, D. Magnesium and magnesium-silicide coated silicon nanowire composite anodes for lithium-ion batteries. *J. Mater. Chem. A* **2013**, 1, 1600-1612.

(52) Ji, L.; Gu, M.; Shao, Y.; Li, X.; Engelhard, M. H.; Arey, B. W.; Wang, W.; Nie, Z.; Xiao, J.; Wang, C. Controlling SEI formation on SnSb‐porous carbon nanofibers for improved Na ion storage. *Adv. Mater.* **2014**, 26, 2901-2908.

(53) Zhang, F.; Xiong, P.; Guo, X.; Zhang, J.; Yang, W.; Wu, W.; Liu, H.; Wang, G. A nitrogen, sulphur dual-doped hierarchical porous carbon with interconnected conductive polyaniline coating for high-performance sodium-selenium batteries. *Energy Storage Mater.* **2019**, 19, 251-260.

(54) Ye, H.; Yin, Y.-X.; Zhang, S.-F.; Guo, Y.-G. Advanced Se–C nanocomposites: a bifunctional electrode material for both Li–Se and Li-ion batteries. *J. Mater. Chem. A* **2014**, 2.

(55) Zhang, J.; Xu, Y.; Fan, L.; Zhu, Y.; Liang, J.; Qian, Y. Graphene–encapsulated selenium/polyaniline core–shell nanowires with enhanced electrochemical performance for Li–Se batteries. *Nano Energy* **2015**, 13, 592-600.

(56) Föppl, H.; Busmann, E.; Frorath, F. K. Die Kristallstrukturen von α‐Na2S2 und K2S2, β‐Na2S2 und Na2Se2. *Z. Anorg. Allg. Chem.* **1962**, 314, 12-20.

(57) Zintl, E.; Harder, A.; Dauth, B. Gitterstruktur der oxyde, sulfide, selenide und telluride des lithiums, natriums und kaliums. *Z Elektrochem.* **1934**, 40, 588-593.
(58) Bommier, C.; Mitlin, D.; Ji, X. Internal structure – Na storage mechanisms – Electrochemical performance relations in carbons. *Prog. Mater Sci.* **2018**, 97, 170-203.
(59) Xie, H.; Tan, X.; Luber, E. J.; Olsen, B. C.; Kalisvaart, W. P.; Jungjohann, K. L.; Mitlin, D.; Buriak, J. M. β-SnSb for Sodium Ion Battery Anodes: Phase Transformations Responsible for Enhanced Cycling Stability Revealed by In Situ TEM. *ACS Energy Lett.* **2018**, 3, 1670-1676.
(60) Orion, I.; Rocha, J.; Jobic, S.; Abadie, V.; Brec, R.; Fernandez, C.; Amoureux, J.-P. Solid-state tellurium-125 nuclear magnetic resonance studies of transition-metal ditellurides. *J. Chem. Soc., Dalton Trans.* **1997**, 3741-3748.
(61) Collins, M. J.; Ripmeester, J. A.; Sawyer, J. F. CP/MAS tellurium-125 NMR in solids: an example of 125Te-35, 37Cl J coupling. *J. Am. Chem. Soc.* **1987**, 109, 4113-4115.
(62) Huff, L. A.; Rapp, J. L.; Baughman, J. A.; Rinaldi, P. L.; Gewirth, A. A. Identification of lithium–sulfur battery discharge products through 6Li and 33S solid-state MAS and 7Li solution NMR spectroscopy. *Surf. Sci.* **2015**, 631, 295-300.
(63) Leskes, M.; Moore, A. J.; Goward, G. R.; Grey, C. P. Monitoring the electrochemical processes in the lithium–air battery by solid state NMR spectroscopy. *J. Phys. Chem. C* **2013**, 117, 26929-26939.
(64) Bryce, D. L.; Bernard, G. M.; Gee, M.; Lumsden, M. D.; Eichele, K.; Wasylishen, R. E. Practical aspects of modern routine solid-state multinuclear magnetic resonance spectroscopy: one-dimensional experiments. *Can. J. Anal. Sci. Spectros.* **2001**, 46, 46-81.
(65) Charpentier, T. The PAW/GIPAW approach for computing NMR parameters: A new dimension added to NMR study of solids. *Solid State Nucl. Magn. Reson.* **2011**, 40, 1-20.
(66) Bonhomme, C.; Gervais, C.; Babonneau, F.; Coelho, C.; Pourpoint, F.; Azais, T.; Ashbrook, S. E.; Griffin, J. M.; Yates, J. R.; Mauri, F. First-principles calculation of NMR parameters using the gauge including projector augmented wave method: a chemist's point of view. *Chem. Rev.* **2012**, 112, 5733-5779.
(67) Perras, F. d. r. A.; Bryce, D. L. Multinuclear magnetic resonance crystallographic structure refinement and cross-validation using experimental and computed electric

field gradients: Application to Na2Al2B2O7. *J. Phys. Chem. C* **2012**, 116, 19472-19482.

(68) Perras, F. A.; Korobkov, I.; Bryce, D. L. NMR crystallography of sodium diphosphates: combining dipolar, shielding, quadrupolar, diffraction, and computational information. *CrystEngComm* **2013**, 15, 8727-8738.

(69) Al-Johani, H.; Abou-Hamad, E.; Jedidi, A.; Widdifield, C. M.; Viger-Gravel, J.; Sangaru, S. S.; Gajan, D.; Anjum, D. H.; Ould-Chikh, S.; Hedhili, M. N. The structure and binding mode of citrate in the stabilization of gold nanoparticles. *Nat. Chem.* **2017**, 9, 890.

(70) Uebersfeld, J.; Etienne, A.; Combrisson, J. Paramagnetic resonance, a new property of coal-like materials. *Nature* **1954**, 174, 614.

(71) Chang, T.; Guo, Q.; Hao, H.; Wu, B.; Yang, Y. Formation of radicals in coal pyrolysis examined by electron spin resonance. *AIP Advances* **2017**, 7, 095303.

(72) Clore, G. M.; Iwahara, J. Theory, practice, and applications of paramagnetic relaxation enhancement for the characterization of transient low-population states of biological macromolecules and their complexes. *Chem. Rev.* **2009**, 109, 4108-4139.

TOC

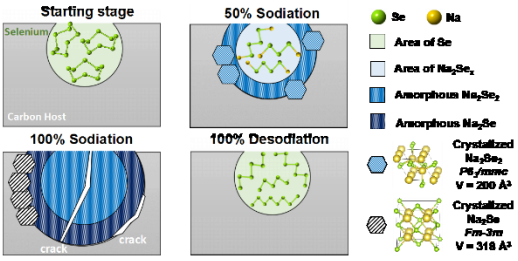
Starting stage
Selenium
Carbon Host
50% Sodiation
100% Sodiation
crack
crack
100% Desodiation
Se
Na
Area of Se
Area of Na_2Se_x
Amorphous Na_2Se_2
Amorphous Na_2Se
Crystallized
Na_2Se_2
$P6_3/mmc$
V = 200 Å³
Crystallized
Na_2Se
$Fm\text{-}3m$
V = 318 Å³